Journal of Structural Biology **133,** 32–42 (2001)
doi:10.1006/jsbi.2001.4330, available online at http://www.idealibrary.com on IDEAL®

Fourier Amplitude Decay of Electron Cryomicroscopic Images of Single Particles and Effects on Structure Determination

Ali Saad,*[,1] Steven J. Ludtke,* Joanita Jakana,* Frazer J. Rixon,† Hiro Tsuruta,‡ and Wah Chiu*

**National Center for Macromolecular Imaging, Verna and Marrs McLean Department of Biochemistry and Molecular Biology, Baylor College of Medicine, Houston, Texas 77030; †Medical Research Council Virology Unit, Institute of Virology, Glasgow G11 5JR, Scotland; and ‡SSRL/SLAC, Stanford University, P.O. Box 4349, MS69, Stanford, California 94309*

Received November 14, 2000, and in revised form January 17, 2001; published online March 21, 2001

Several factors, including spatial and temporal coherence of the electron microscope, specimen movement, recording medium, and scanner optics, contribute to the decay of the measured Fourier amplitude in electron image intensities. We approximate the combination of these factors as a single Gaussian envelope function, the width of which is described by a single experimental B-factor. We present an improved method for estimating this B-factor from individual micrographs by combining the use of X-ray solution scattering and numerical fitting to the average power spectrum of particle images. A statistical estimation from over 200 micrographs of herpes simplex virus type-1 capsids was used to estimate the spread in the experimental B-factor of the data set. The B-factor is experimentally shown to be dependent on the objective lens defocus setting of the microscope. The average B-factor, the X-ray scattering intensity of the specimen, and the number of particles required to determine the structure at a lower resolution can be used to estimate the minimum fold increase in the number of particles that would be required to extend a single particle reconstruction to a specified higher resolution. We conclude that microscope and imaging improvements to reduce the experimental B-factor will be critical for obtaining an atomic resolution structure.

Key Words: **amplitude decay B-factor; electron cryomicroscopy; X-ray solution scattering; single particle; structure; virus; contrast transfer function.**

INTRODUCTION

Electron cryomicroscopy is a structural technique that has been used to determine the tertiary structure of biological macromolecules that can form a highly ordered 2-dimensional crystal (Henderson *et al.*, 1990; Kühlbrandt *et al.*, 1994; Nogales *et al.*, 1998; Murata *et al.*, 2000). In these specimens, amplitudes of the structure factor were obtained from electron diffraction intensities while phases were derived from images. For noncrystalline specimens it is impractical to obtain useful electron diffraction intensities. Therefore, one would retrieve both amplitudes and phases directly from images. However, the accuracy of such retrieval requires more elaborate data processing, because a number of experimental and instrumental factors must be properly included in the data treatment. These factors include the contrast transfer function (CTF) of the microscope (Erickson and Klug, 1970; Thon, 1971), the effective envelope function (E) (Hanszen, 1971; Frank, 1973, 1976; Wade and Frank, 1977; Downing and Chiu, 1982; Brink and Chiu, 1991; Wade, 1992), and a background noise function (N) (Glaeser and Downing, 1992; Zhu *et al.*, 1997; Ludtke *et al.*, 1999).

Because of advances in experimental and computational techniques, the resolution of single particle reconstructions has reached beyond 9 Å (Böttcher *et al.*, 1997; Conway *et al.*, 1997; Trus *et al.*, 1997; Matadeen *et al.*, 1999; Mancini *et al.*, 2000; Zhou *et al.*, 2000). In order to extend the analysis toward atomic resolution, it will be necessary to include many more particle images containing high-resolution information (Henderson, 1995; Glaeser, 1999; Thuman-Commike *et al.*, 1999). Unlike with crystalline specimens, it is generally difficult to determine quantitatively the quality of images of ice-embedded single particles in terms of the contrast above the background at different resolutions. As well as assessing quality, it would also be desirable to have an

[1] Current address: King SAUD University, College of Applied Medical Sciences, Department of Biomedical Technology, P.O. Box 10219, Riyadh 11433, Saudi Arabia.

1047-8477/01 $35.00

experimentally based method for making rough estimates of the relative numbers of particle images needed to achieve specific higher resolution reconstructions. This study describes an improved version of a quantitative method (Thuman-Commike *et al.*, 1999) for analyzing images of ice-embedded single particles using data from the herpes simplex virus type-1 (HSV-1) B capsid as an illustrative example. Our approach is to combine the X-ray solution scattering intensity of the particles with computational fitting to the average power spectrum of the particle images in a single micrograph to determine the parameters in the functions: CTF, E, and N, which would influence the image contrast.

METHODS

Electron Cryomicroscopy

Purified HSV-1 B capsids were embedded in vitreous ice suspended across the holes in holey carbon grids for electron cryomicroscopy observation following established procedures (Zhou *et al.*, 2000). A JEOL4000 electron cryomicroscope operating at 400 kV with a LaB_6 filament was used for the image data collection. The C_s of the objective lens pole piece is 4.1 mm. A 100-μm condensor aperture and 70-μm objective aperture were used. Flood beam illumination with a condensor spot size of 3 and a beam diameter of ~2.6 μm was set to allow the recording of images at 50 000× magnification with a specimen dose of 10–15 electrons/Å^2 and an exposure time of 1 s. Microscope alignment, specimen assessment, and focusing were performed using a Gatan (Pleasanton, CA) 1 k × 1 k slow-scan charge-coupled device camera. All micrographs were recorded on Kodak SO163 film, which was developed in a D19 developer at 20°C. Micrographs were digitized on a Zeiss SCAI scanner (Carl Zeiss, Englewood, CO) at a step size of 7 μm/pixel and subsequently averaged to 10.5 μm/pixel. Particle images (656 × 656 pixels) were selected manually.

X-Ray Solution Scattering

X-ray solution scattering experiments were conducted at beam Line 4-2 of the Stanford Synchrotron Radiation Laboratory using a significantly upgraded version of the Biotechnology Resources small angle scattering/diffraction instrument (Tsuruta *et al.*, 1998). The synchrotron radiation beam was produced by a wiggler, focused with a bent cylindrical mirror, and monochromatized with a double-crystal Si (111) monochromator. The beam energy was calibrated to 8333 eV (wavelength 1.488 Å) at the NiK absorption edge. The linear, position sensitive proportional counter, EMBL-BioLogic Model No. 210 (Grenoble, France), was filled with Xe/CO_2 and was interfaced to the beam line computer with a set of fast encoding electronic modules. The sample-to-detector distance was determined using the (100) diffraction peak from cholesterol myristate powder. The (100) peak position was determined to be 50.1 ± 0.1 Å using a Fuji BAS-V image plate scanned by a Fuji BAS2000 off-line scanner with a 100-μm pixel size.

Samples of HSV-1 capsid particles at concentrations between 20 and 50 mg/ml were contained in polycarbonate sample cells equipped with 25-μm-thick mica windows and maintained at a constant temperature (20 ± 1°C) during data collection. The total exposure time for each sample ranged from 10 to 20 min, subdivided into 5 to 15 separate measurements in order to monitor scattering intensity changes due to potential radiation damage. Blank buffer solution scattering measured under conditions identical to those used for the corresponding sample solution was normalized to integrated primary beam intensity and subtracted from the sample solution scattering. All scattering curves for a given sample were corrected for detector channel response and averaged after confirming that radiation damage was negligible.

Experimental B-Factor Estimation

The Fourier transforms of a set of single particle images from a single micrograph were calculated. The Fourier intensities were then averaged rotationally for each particle and over the set of particle images to produce a 1-D power spectrum as a function of spatial frequency, $M^2(s)$ as defined in Eq. (2).

The corrected, background subtracted X-ray scattering intensity provides an isotropically averaged 1-D structure factor function that will be nearly identical to the structure factor function, $F(s)$, of the particle from the electron scattering. If the orientations of single particles in the electron micrograph are not uniformly distributed, the structure factor function may contain some differences from the isotropic value, depending on the degree of anisotropy. While this effect could potentially cause problems, generally it simply results in a mismatch in one or more sharp peaks present at lower resolution, the effect of which can be ignored in the fitting process. For the five different biological specimens to which we have applied this method of analysis, it has not caused a significant problem, even though several of these samples had highly preferred orientations in ice (unpublished results). We also assume that X-ray and electron scattering will produce nearly identical results at the spatial frequencies we are investigating.

Altogether, eight parameters must be determined for Eq. (2): B-factor, defocus, amplitude contrast, a scaling factor, and four background function ($N(s)$) parameters. Parameter estimation was performed using *Ctfit*, part of the EMAN software package (Ludtke *et al.*, 1999). While this fitting process could be automated, currently it is performed manually. The background parameters are determined first. By definition, the background function must pass through all of the zeros of the CTF, and as the envelope function decays to near zero at high resolution, the entire curve asymptotically approaches the background. The amplitude contrast is initially set to ~10% (Thuman-Commike *et al.*, 1999), and the defocus is determined approximately by matching the zeroes of the CTF. The scaling factor and experimental B-factor are then adjusted to match the decay of the curve. The four nonbackground parameters are then iteratively adjusted until a near-optimal fit is achieved.

THEORETICAL BACKGROUND

The Fourier transform of an electron micrograph can be expressed as

$$\mathbf{M}(s, \theta) = \mathbf{F}(s, \theta)\mathrm{CTF}(s)E(s) + \mathbf{N}(s, \theta). \qquad (1)$$

M is the measured quantity, in this case, the complex-valued 2-dimensional (2-D) Fourier transform of the image intensity of a single particle in an electron micrograph, where s and θ represent polar coordinates in Fourier space. $\mathbf{F}(s, \theta)$ is a 2-D slice of the 3-dimensional (3-D) Fourier transform (structure factor function) of the object being imaged (Crowther *et al.*, 1970). The normal of the slice is defined by the 3-D orientation of the object. For simplicity, we assume that astigmatism and drift are negligible. Under this assumption, both the CTF

and the effective envelope function are real-valued functions only of spatial frequency, s. $\mathbf{N}(s, \theta)$ represents additive incoherent background noise with a consistent spectral profile. The physical source of N is not explicitly defined, but it can be attributed to many factors such as inelastic scattering, multiple scattering, ice thickness, and noise from the recording medium and digitizer (Zhu *et al.*, 1997; Ludtke *et al.*, 1999).

In this equation, $\mathbf{M}(s, \theta)$ represents the measured data and $\mathbf{F}(s, \theta)$ represents the true structure factor of the particle, which we wish to obtain. $\mathbf{N}(s, \theta)$ cannot be directly subtracted since it represents random fluctuations. The best we can do is to characterize its spectral profile and rely on sufficient averaging to render the noise level negligible at the desired resolution. Multiple scattering is difficult to compensate for and may affect the accuracy of the reconstruction for thick specimens if no additional corrections are made. CTF(s) and $E(s)$, however, must be determined as accurately as possible for accurate determination of $\mathbf{F}(s, \theta)$. CTF(s) is oscillatory and causes phase flipping at specific spatial frequencies. Failure to correct the CTF accurately can produce significant mass misplacements in the 3-D reconstruction, such as the exaggeration of holes and protrusions. Various methods for making CTF corrections during the 3-D reconstruction of single particles have been introduced (for instance, Böttcher *et al.*, 1997; Trus *et al.*, 1997; Zhu *et al.*, 1997; Conway and Steven, 1999; Ludtke *et al.*, 1999; Matadeen *et al.*, 1999; Zhou *et al.*, 2000). Improper correction of E(s) will lead to either a model in which real features are not resolvable or one in which noisy features are unduly magnified.

To determine CTF(s), $E(s)$, and $\mathbf{N}(s, \theta)$ it is convenient to examine the power spectrum, e.g., the average of the Fourier intensities of a large set of particles from the same micrograph. Since we are only interested in the power spectrum of $\mathbf{N}(s, \theta)$, and CTF(s) and $E(s)$ are functions of s only, we can rotationally average the 2-D power spectrum. Some mathematical manipulation of Eq. (1) provides Eq. (2), a general description of the radial power spectrum of an electron micrograph (Zhu *et al.*, 1997; Ludtke *et al.*, 1999):

$$M^2(s) = kF^2(s)\mathrm{CTF}^2(s)E^2(s) + N^2(s). \qquad (2)$$

M^2 represents the averaged 1-D power spectrum of a set of particle images, $F^2(s)$ is the rotationally averaged 1-D structure factor function of the measured object, and $N^2(s)$ is the average power spectrum of the incoherent background function. CTF(s) and $E(s)$ are the same as in Eq. (1). k is a scaling factor which maintains the proportionality between the first term and the second term, since micrograph normalization is arbitrary.

Most CTF parameters can be estimated directly from a plot of $M^2(s)$ (Zhou *et al.*, 1996; Ludtke *et al.*, 1999). However, while methods for determining the parameters of different envelope functions of the microscope have been developed (Frank, 1969, 1976), they have not been routinely applied as part of the image reconstruction procedure for ice-embedded particles. A few published single particle reconstructions have attempted to compensate the high frequency damping in the structure factor function by sharpening the reconstruction using a Gaussian function. The width of this Gaussian function is commonly referred to as the B-factor (e.g., Böttcher *et al.*, 1997; Mancini *et al.*, 2000; Zhou *et al.*, 2000). In the context of this paper, we refer to this as the overall B-factor.

In this study, we introduce a procedure for estimating the overall amplitude decay function for an electron micrograph due to experimental and instrumental factors. We also simplify the overall amplitude decay function by approximating it as a simple Gaussian function (Glaeser and Downing, 1992; Thuman-Commike *et al.*, 1999) with only one parameter to be determined (henceforth called the experimental B-factor), as shown in Eq. (3).

$$E(s) = e^{-Bs^2} \qquad (3)$$

Note that this experimental B-factor is not the same as the overall B-factor, used by other investigators, which is generally empirical and compensates both for the experimental B-factor and the computational B-factor (i.e., amplitude decays caused by particle orientation errors, and other computational artifacts (Conway and Steven, 1999)). The expression in Eq. (3) has the same form as the temperature factor used in X-ray crystallography to describe atomic vibrations within crystals. However, the physical origin for the experimental B-factor in electron microscopy is related to microscope optics and experimental conditions, such as motion of the entire sample during measurement. While atomic vibrations are also included in this B-factor, their effect is negligible compared to the others.

We further define CTF(s) and $N(s)$ in Eq. (2) as

$$\mathrm{CTF}(s) = -(\sqrt{1 - Q^2}\sin(\gamma) + Q\cos(\gamma)),$$

where

$$\gamma = 2\pi\left(-\frac{C_s\lambda^3 s^4}{4} + \frac{\Delta Z\lambda s^2}{2}\right), \quad 0 <= Q <= 1, \quad (4)$$

and

$$N^2(s) = n_1 e^{n_2 + n_3 s^2 + n_4 \sqrt{s}}. \quad (5)$$

CTF(s) is the well-known contrast transfer function with the parameters Q, C_s, λ, and ΔZ defined as fractional amplitude contrast, spherical aberration coefficient, electron wavelength, and defocus, respectively. With this convention, a positive value of ΔZ represents underfocus (Erickson and Klug, 1970). The expression for $N^2(s)$ is empirical and has worked well on data from several microscopes. However, any expression which accurately fits the background may be substituted.

In the present study, we combine X-ray solution scattering data with a theoretical model of the CTF, a Gaussian envelope function, and a four-parameter empirical background model. By completely fitting the radially averaged Fourier intensity, we obtain an estimate for the experimental B-factor of each micrograph, using *ctfit*, the graphical CTF determination program in EMAN (Ludtke *et al.*, 1999). This technique provides a mechanism for routine evaluation of electron micrographs of ice-embedded single particles of HSV-1 B capsids before progressing to a full 3-D reconstruction. Furthermore, a statistical estimation of the typical experimental B-factor in over 170 micrographs was used to estimate the minimum number of particles that would be required for a 3-D reconstruction toward a resolution beyond 8 Å.

RESULTS

Experimental Data from X-Ray Solution Scattering and Electron Cryomicroscopy

Figure 1a shows the entire frequency range of X-ray scattering intensities ($I_x(s)$) of HSV-1 B capsids. This curve is a composite of two sets of readings taken at different detector positions. In the low-angle curve (Fig. 1b), a peak is present at about 66–80 Å spacing, indicating the presence of many structural features at this length scale in the capsid. In the small angle curve (Fig. 1a), broad peaks are seen at around 10 and 5 Å, reflecting the presence of alpha helices and beta strands in the structure (Thuman-Commike *et al.*, 1999).

Figure 2a shows a portion of an electron micrograph of HSV-1 B capsids taken with a defocus value of 0.6 μm, while Fig. 2b shows the average power spectrum computed from the Fourier transform intensities of selected particles in this micrograph. In this figure, it appears that the CTF rings in the power spectrum extend to 7 Å resolution.

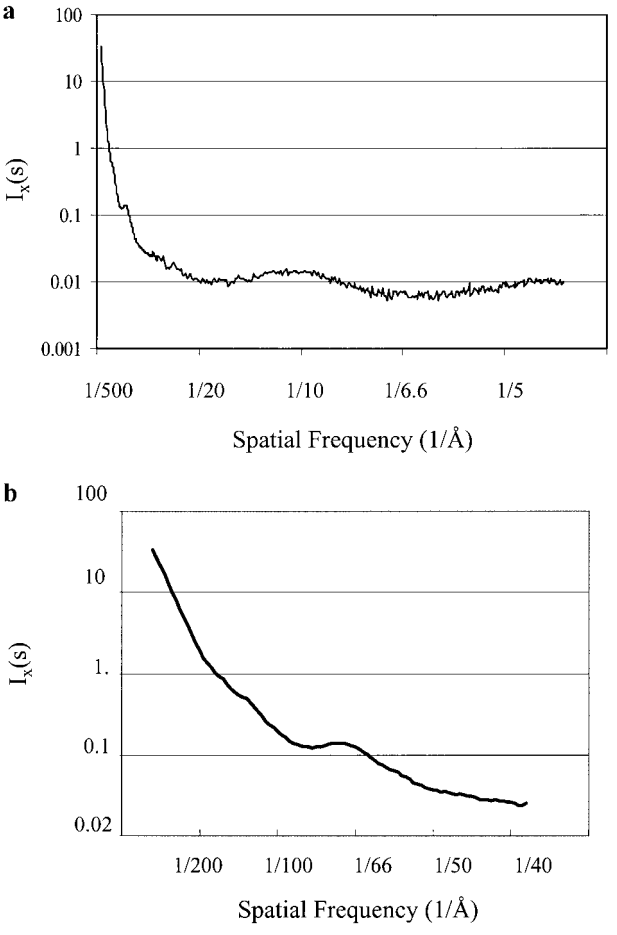

FIG. 1. X-ray solution scattering intensity ($I_x(s)$) of a HSV-1 B capsid suspension. The curve in (a) is a composite of data recorded at two different camera settings of 1.0 and 0.3 m from the specimen. The curve in (b) shows an expansion of the low-resolution part of the scattering curve. Both curves are plotted on linear scales with arbitrary units.

Determination of Detectable Contrast and Experimental B-Factor of Images

The image quality in terms of detectable signal in Fourier space was assessed quantitatively by evaluating the CTF rings visualized in the average power transform of particle images using *ctfit*. Any images that exhibited obvious drift or astigmatism as evident in the initial inspection of the average power spectrum as shown in Fig. 2a were excluded from further analysis. Therefore, we could apply the analytical formulation as defined in Eqs. (2–5). Figure 3a shows the 1-D power spectrum generated from Fig. 2b. Equation (2) is fitted to this curve using the measured X-ray scattering curve. The overall fit and the background function $N(s)$ are overlaid on the power spectrum in Fig. 3a. For quantitative assessment, the detectable contrast ($C(s)$)

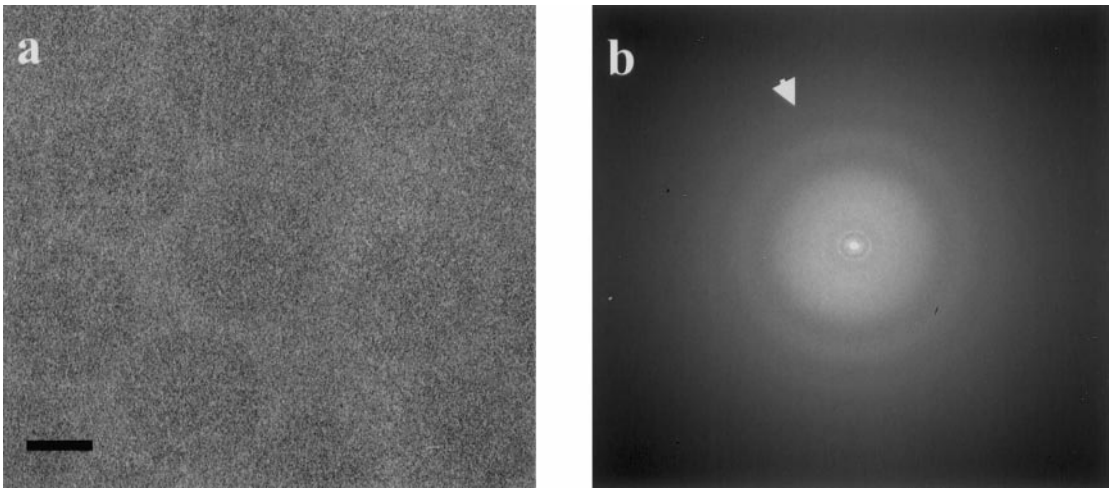

FIG. 2. (a) A 400-kV electron image of HSV-1 B capsids (1250 Å in diameter). Scale bar = 500 Å. (b) Average power spectrum of 65 particle images. The arrowhead shows a CTF ring at 7 Å resolution.

above the background, as defined in Eq. (6), is calculated as a function of spatial frequency for each micrograph (Fig. 3b).

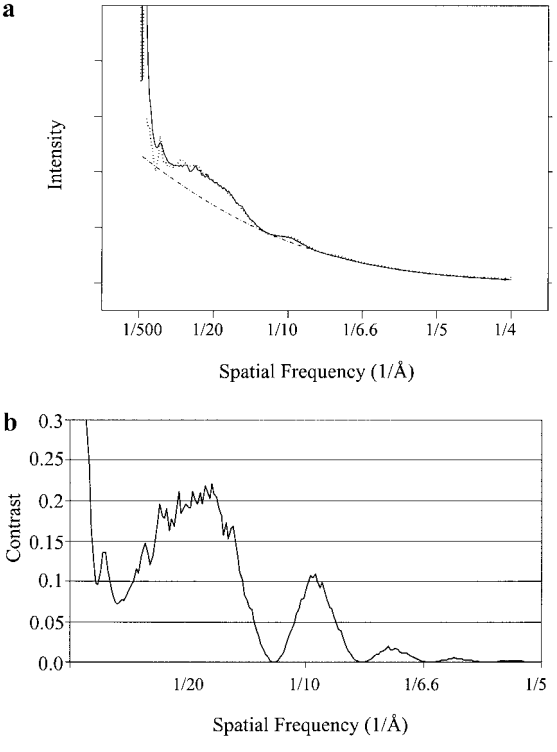

FIG. 3. (a) Analysis of the average power spectrum from Fig. 2b plotted on an arbitrary linear scale. The dashed line shows the circularly averaged Fourier intensities. The dot–dashed line is the fitted noise curve. The solid line represents the fitted curve generated using Eq. (2). (b) The contrast is plotted as a function of the spatial frequency of the circularly averaged Fourier intensity using Eq. (6). The parameters in CTF, E, and N are determined from the *ctfit* program.

$$C(s) = (I_x(s)\mathrm{CTF}^2(s)E^2(s))/N^2(s) \qquad (6)$$

This plot clearly reveals the zeros of the CTF and the actual fall off in the Fourier intensity of the micrograph, recorded in our 400-kV cryomicroscope. The contrast of the image data at 7 Å is ~2%, which is typical of the better micrographs from this data set.

Experimental B-Factor Variation for a Single Specimen

To assess the quality of our data, as well as that of the microscope itself, we examined the distribution of experimental B-factors in micrographs taken at similar and different defocus settings. Figure 4 shows the histogram of the experimental B-factor estimated from 170 micrographs, which have a defocus range of 0.5–2.0 μm, taken using a single preparation of HSV-1 B capsids. These micrographs, which were used for the final 3-D reconstruction,

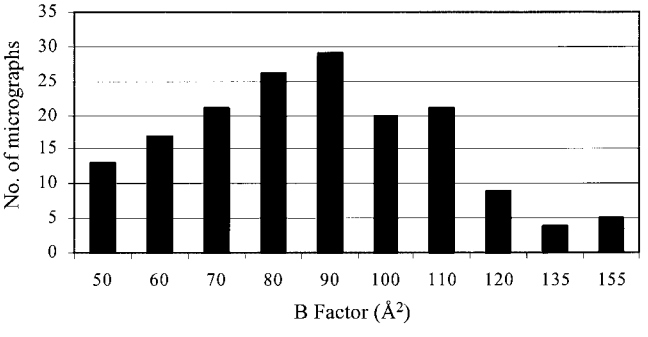

FIG. 4. Histogram of the experimental B-factors (in Å^2) of 170 micrographs of HSV-1 capsids recorded over a defocus range of 0.5–1.6 μm on a JEOL 400-kV electron cryomicroscope. The B-factor values span from 50 to 160 Å^2 with a peak at ~90 Å^2.

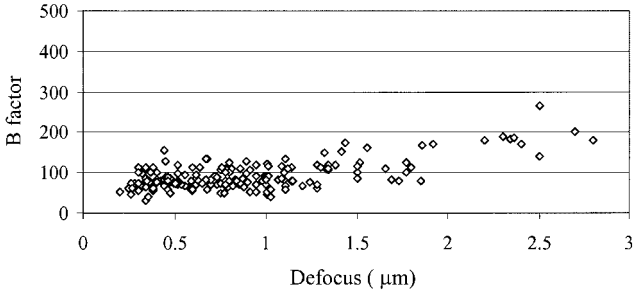

FIG. 5. Experimental B-factors (in Å^2) of 240 micrographs of HSV-1 B capsids plotted as a function of defocus value showing the roughly linear dependence between B-factor and defocus which is above 1 μm.

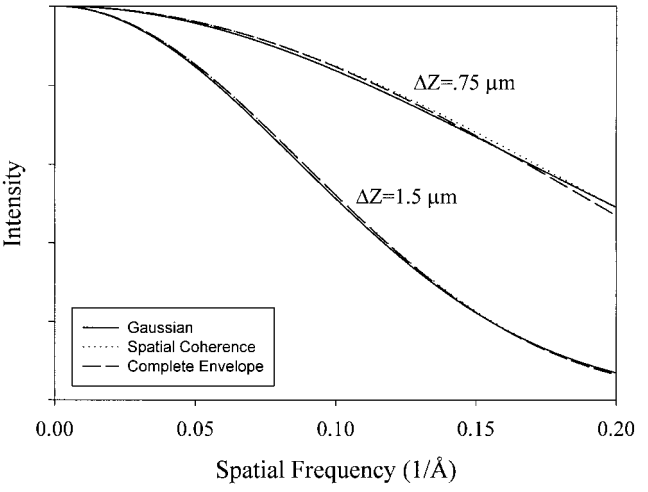

FIG. 6. Demonstration of the accuracy of the Gaussian approximation at two different defocuses at 400 kV and a spherical aberration coefficient of 4.1 mm. The complete envelope function (dashed lines) consists of terms for spatial coherence (semi-angle of illumination = 0.12 mrad), temporal coherence (2 eV spread), and objective lens stability (2 ppm). The three curves at each defocus are nearly indistinguishable. Using these values close to our imaging conditions, the spatial coherence (dotted lines) term clearly dominates, and the Gaussian approximation (solid lines) is clearly quite valid. These curves are plotted on arbitrary linear scales.

were selected from a larger set (Zhou *et al.,* 2000). The experimental B-factor varies from 50 to 160 Å^2 with a peak at ~90 Å^2. This type of information provides a statistical measure (average and standard deviation) of the quality of the overall data set.

Since the amplitude decay can be influenced by a number of experimental conditions, we tried to verify our approximation of the decay function by examining a larger data set of micrographs (240 photographs) with a broader range of defocuses. Figure 5 shows the experimental B-factor as a function of defocus. The experimental B-factor is significantly lower in the closer to focus images (left part of the curve in Fig. 5). The variation of the experimental B-factor at similar defocuses, as shown by the degree of scatter in the curve, is considerably less than the defocus dependent variation. From this observation, we conclude that, as expected, there is a positive correlation between the defocus value and the experimental B-factor value.

The only envelope function of the electron microscope which depends on the defocus of the image is spatial coherence (Hanszen and Trepte, 1971; Frank, 1973; Wade and Frank, 1977; Brink and Chiu, 1991), which also depends strongly on the semi-angle of illumination. Figure 6 shows how the spatial coherence envelope function (dotted lines) varies with defocus for a specific semi-angle of illumination of 0.12 mrad. This value, which was used in our experiments, was predetermined in a separate experiment by measuring the width of the diffraction spots of a gold crystal (Williams and Carter, 1996). Such an illumination angle is the smallest possible value, which still allows sufficient brightness for recording an image in a short exposure time (1 s), while ensuring maximum possible coherence of the incident electrons. In addition to the spatial coherence effect, the other well-known envelope functions for the electron microscope are temporal coherence and specimen movement (Chiu, 1978). The temporal coherence is affected by fluctuations in the electron voltage and in the objective lens current. These are on the order of 2–5 ppm in our microscope (Brink and Chiu, 1991). The extent of vertical movement of the specimen (or cryostage) is unknown but was estimated from a separate experiment using carbon film as a test specimen, to be less than 300 Å for data with 6–9 Å resolution. Under the imaging conditions used in our microscope and the resolution range in our data, the dominant factor affecting the Fourier amplitude fall off is spatial coherence. This is clearly shown in Fig. 6 by the good match among the spatial coherence envelope function (dotted lines), the composite envelope function (dashed lines), and the Gaussian approximation (solid lines) at two different defocuses.

TABLE I

Influence of B-Factor Values on the Estimated Minimum Number of Particles Required for 3-D Reconstruction of HSV-1 Capsids at Different Resolutions

Resolution	8.5 Å	7.5 Å	6.0 Å	5.0 Å	4.5 Å
B = 50 Å^2	3000	7000	20 000	50 000	150 000
B = 100 Å^2	6000	19 000	170 000	1 200 000	5 000 000

Note. In this estimate, the B-factor effect due to computational errors is ignored.

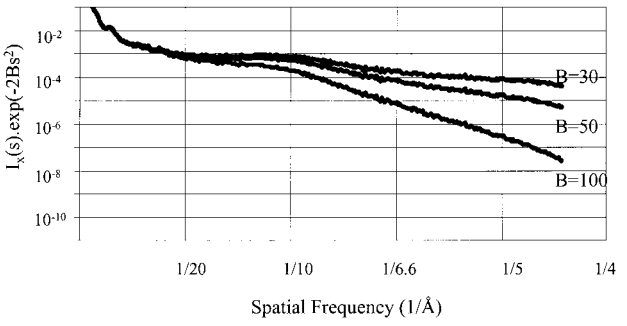

FIG. 7. Simulation showing the decay of the Fourier intensity of electron micrograph as a function of spatial frequency resulting from the fall off of the structure factor function as represented by the X-ray scattering intensity ($I_x(s)$) and three different B-factor values (30, 50, and 100 Å^2).

These matches validate our approach in using this approximation (Eq. 3) for the effective envelope function in our image data set.

Estimating Particle Requirements for 3-D Reconstruction at Higher Resolution

The relative number of particles required for 3-D reconstructions at different resolutions depends on the structure factor function of the object and the overall B-factor. Figure 7 shows the predicted decay of the Fourier intensity of electron micrographs as determined by multiplying the X-ray solution scattering intensity of the HSV-1 B capsids with the effective envelope function approximated by the Gaussian function with different B-factors. For simplicity, we assume that the overall and experimental B-factors are equivalent. About 6000 particles were used to reconstruct the HSV-1 B-capsid to 8.5 Å resolution (Zhou *et al.,* 2000). This number of particles was determined empirically. A similar number of particles was used for the 7.5 Å reconstruction of the hepatitis B virus core (Böttcher *et al.,* 1997). Based on this empirical number and using the plot in Fig. 7, we can predict the minimum increase in the number of HSV-1 particles required for 3-D reconstruction at higher resolutions for two B-factor values. As shown in Table I, the relative number of particles required increases very rapidly beyond 6 Å. Clearly, improvements in the overall B-factor become increasingly important at higher resolutions.

DISCUSSION

Several structures of icosahedral viruses have been resolved to 7–9 Å, using electron cryomicroscopy (Böttcher *et al.*, 1997; Conway *et al.*, 1997; Trus *et al.*, 1997; Mancini *et al.,* 2000; Zhou *et al.,* 2000). For the amplitudes of the structure factor function in the final map to be correct, an inverse Gaussian filter must be applied using an overall B-factor. Ideally, an experimental B-factor correction would be made independently for each micrograph, possibly followed by an empirical correction to the final model. In some high-resolution virus particle reconstructions, a single empirically determined overall B-factor was used for correcting the final 3-D model (Table II), with no corrections being applied to the individual micrographs. It should be noted that these two approaches do not produce equivalent results. The experimental B-factor correction combined with a scaling factor correction, when applied to each micrograph, ensure that micrographs contribute to the final model in proportion to the relative contrast present at each resolution in each image, which may vary considerably from micrograph to micrograph, especially at high resolution. Carrying out such individual corrections may become necessary for accurate high-resolution ($<$7 Å) structure determination of single particles in general.

One note of caution, however, the overall B-factor has been defined in two different ways in the literature. The definition used in X-ray crystallography and some, but not all, electron microscopy literature produces B-factors four times larger than those produced by the definition used here. Unfortunately, the literature is not always explicit about which definition is being used. The broad variation of overall B-factors as shown in Table II could be due to differences in instrumental performance, image quality, and computational errors. However, none of these studies reported a quantitative determination of the experimental B-factor as is described here. The overall B-factors in Table II incorporate not only the effective envelope functions due to experimental factors, but also include the effects of inaccurate orientation determination and other computational artifacts produced by the reconstruction procedure (i.e., computational B-factor). In this paper, we determine the amplitude decay factor solely due to experimental factors. Therefore, our experimental B-factor would be expected to have a lower value than the overall B-factor typically used for correcting the final reconstruction. It is indeed the case that the average experimental B-factor of the HSV-1 B capsid determined here is about half of the overall B-factor (180 Å^2) used for the final 3-D reconstruction (Zhou *et al.,* 2000).

For high-resolution structure determination, sufficient contrast at the desired resolution must be present in the image data. Although contrast adds linearly in a 3-D reconstruction when proper CTF correction is applied, very low contrast may be insufficient for accurate orientation determination. For this reason, once the contrast falls below some value defined by the specific alignment algorithm

TABLE II
Overall B-Factors Used in High-Resolution Icosahedral Virus Reconstructions

Virus	Microscope gun type	Overall B-factor (Å^2)	References
Hepatitis B core	Hitachi HF2000-FEG	500	(Böttcher *et al.*, 1997)
Hepatitis B core	Philips CM12-FEG	100	(Conway *et al.*, 1999)
HSV-1 B capsid	JEOL4000EX-LaB_6	180[a]	(Zhou *et al.*, 2000)
Semliki Forest virus	Philips CM200-FEG	15	(Mancini *et al.*, 2000)

[a] The B-factor is defined as in this paper and is equivalent to 720 Å^2 under the definition used for the other data in this table.

being used, the data at higher resolution become less reliable. In this paper, we address the issue of how we assess the individual image data quality of ice-embedded single icosahedral particles. Such an analysis is a useful tool for investigators to estimate the potential structural information they can expect to retrieve from the data on hand and should be generally applicable to any micrograph of single particles with or without internal symmetry.

Quantitative Evaluation of Micrograph Quality

Image contrast is affected by the type of electron microscope used and various experimental factors. Theoretical forms exist for several envelope functions for the electron microscope, including spatial and temporal coherence and specimen movement in both vertical and horizontal directions (Hanszen and Trepte, 1971; Frank, 1973; Wade and Frank, 1977; Brink and Chiu, 1991). These functions have the analytical forms of exponential, Gaussian, Bessel, or sinc functions (Chiu, 1978). While it might be desirable to parameterize each of these envelope functions to gain clearer insights into the specific mechanisms responsible for resolution limiting factors, in our experience the available data are not sufficient to determine uniquely all of the necessary parameters. Empirical evidence has shown that a one-parameter model is typically sufficient to describe an effective envelope function at the intermediate resolution studied here (Fig. 6). It should be pointed out that this parameterization might need to be expanded for higher resolution data from an electron microscope with a better spatial coherence.

In our analysis, we take advantage of the availability of X-ray solution scattering data for the particles in suspension (Fig. 1). Such measurement is relatively easy to perform, provided that a specimen of sufficient particle concentration can be prepared. Once the 1-D structure factor function is known, determining the experimental B-factor for each micrograph, using the tools provided as a part of the EMAN package, is a straightforward process. Based on our experience, a significantly different experimental B-factor value may be obtained if a less accurate definition of the background function ($N(s)$) is employed. Our early analysis of P22 phage images (Thuman-Commike *et al.*, 1999) recorded under similar electron microscopic conditions resulted in higher experimental B-factors than those reported here. In that case, the background function was determined by calculating the power spectrum of ice in areas near the particles. However, due to variations in ice thickness across the specimen, as well as the exclusion of ice volume by the molecules in boxed out particles, this choice would not be as accurate as the method described here, where the background is fit directly.

Experimental B-factor estimation using X-ray scattering data prior to performing the elaborate processing required to compute a 3-D structure serves two purposes. First, the B-factor of a micrograph provides a quantitative measure of its quality in a specimen-independent way. As shown in Fig. 5, the same defocus can yield a spread of experimental B-factors for a given specimen under similar electron imaging conditions. Furthermore, there is still a significant amount of amplitude fall off even at small defocus values at which the spatial coherence effect should not have a major effect. Therefore, it is important to prescreen the data by determining the experimental B-factor for each micrograph prior to merging it with other data. Because the high B-factor micrographs do not contribute to the high-resolution data, and there is no need for additional low-resolution information, any micrographs with an unusually high experimental B-factor for a given defocus value can be excluded from the reconstruction. Second, when striving for a higher resolution reconstruction, one may use the experimental B-factor as a quantitative indicator to evaluate the potential of different experimental conditions and/or instruments for achieving the desired resolution. An unusually high experimental B-factor in the analysis of the images should signal the experimentalist to change the imaging conditions and/or consider the use of a different instrument.

In this paper, we demonstrate the feasibility of routinely estimating the experimental B-factor for every micrograph. The histogram in Fig. 4 represents the statistical distribution of B-factors of 170

micrographs that were used for a 3-D reconstruction of the HSV-1 B-capsid at 8.5 Å resolution. The mean value of the experimental B factor is ~90 Å^2 and the upper limit is ~160 Å^2, exhibiting a positive correlation with increasing defocus (Fig. 5). By examining the characteristics of the various known envelope functions with the parameters used in our experiment, we conclude that the defocus-dependent portion of the observed change in experimental B-factor is due to spatial coherence. This defocus-dependent effect is more pronounced due to the use of a LaB_6 filament in our JEOL4000 electron cryomicroscope. While the spatial coherence could be improved through use of a smaller aperture, this would decrease beam intensity and require longer exposure times, with a consequential dramatic increase in the observed drift in the images. A field emission gun produces a more parallel beam without sacrificing beam brightness. Therefore, in order to improve our image data quality, we should consider using an electron microscope with a field emission gun (Zhou *et al.*, 1993).

Micrograph Corrections

There are several reasons why, in order to perform robust amplitude and phase CTF corrections, it is necessary to collect data over a range of defocuses. First, the very close to focus micrographs (0.2 to 0.5 μm taken in our JEOL 4000 electron cryomicroscope (Brink and Chiu, 1991)) provide excellent signal to noise ratios at high resolution, but supply very little low-resolution information which is still necessary for a complete reconstruction. In addition, close to focus images have lower contrast, making accurate orientation determination more difficult. Second, generally only one zero of the CTF is present in such close to focus micrographs (which makes the CTF parameter estimation less accurate). Far from focus micrographs provide excellent overall signal to noise ratio and sufficient information at low resolution for accurate amplitude correction. Unfortunately, since the experimental B-factor is strongly dependent on the defocus as shown in Fig. 5, such far from focus micrographs often contain very little high-resolution information. This effect is particularly pronounced on microscopes without field-emission guns, such as the JEOL 4000 intermediate voltage microscope (Brink and Chiu, 1991), which was used to collect the data discussed in this paper.

The orientation refinement of a single particle must include data beyond the first zero of the CTF. In general, both the phase residual and the correlation coefficient used to determine the orientation parameters deteriorate rapidly at high spatial frequencies. Having the detectable contrast plot (such as Fig. 3b) for each micrograph would provide an additional constraint, or weighting factor, when evaluating the refinement of the orientation parameters.

Estimating the Minimum Increase in Number of Particles Required for Higher Resolution Reconstruction

The methodology for retrieving a low-resolution 3-D model from single particles is relatively straightforward. However, it is difficult, in general, to make a good estimate of the amount of data that would be required to achieve a reconstruction beyond 7–9 Å. The conventional geometrical relationship among the number of particles, particle size, and resolution is oversimplistic. However, all theoretical estimates based on experiences to date with 2-D crystals acknowledge that this will require a substantial increase for single particle reconstruction due to the rapid fall off in contrast at high resolution (Henderson, 1995; Glaeser, 1999).

The number of particles required for a 3-D reconstruction at a given resolution is inversely proportional to the total contrast present in the micrograph at that resolution, including both the structure factor intensity function and the effective envelope function (Thuman-Commike *et al.*, 1999). This statement makes several assumptions, including the assumption that particle orientations can be determined exactly, data are evenly distributed in an asymmetric unit, radiation damage is negligible, and the particles are actually identical at the specified resolution. Clearly, these assumptions are not entirely realistic. Furthermore, this analysis applies only to 2-D averages, and an additional geometric factor to account for data completeness in 3-D must also be included for an accurate estimate of particle numbers. Even taking these considerations into account, however, we can still obtain an estimate of the minimum increase in the number of particles that will be required to improve the resolution of reconstruction from an existing lower resolution to a specific higher resolution. This is a relative estimate, so the number of particles that were required to achieve an existing, lower resolution reconstruction must be provided as a parameter to the estimate.

As shown in Fig. 7, with $B = 100$ Å^2, improving the resolution from 10 to 5 Å would require a 500-fold increase in the number of particles. However, with $B = 50$ Å^2, the increase in particle count required is reduced to only 25-fold. This demonstrates that a realistic estimate of the B-factor is crucial for approximating the number of particles that will be required. The predicted numbers of particles needed for the increases in resolution shown in Table I are based on the number of particles required to determine the 8.5-Å HSV-1 B capsid structure (Zhou *et*

al., 2000) and assume that the computational error is negligible. It is well recognized that the actual number of particles needed for any reconstruction at any resolution cannot be accurately predicted. Therefore, the values predicted in Table I are minimum values only and may be off significantly. They depend on the specific algorithms used in reconstruction and the extent of the icosahedral symmetry preserved in the particles at a higher resolution. However, this predicted value is still useful when determining minimum manpower and time requirements and when considering whether the apparatus available is adequate to achieve a given resolution. For example, we estimate that a minimum of 170 000 particles would be required for a 6 Å reconstruction using an overall B-factor of 100 $Å^2$. A further increase to 5 Å would require well over a million particles. This clearly illustrates the difficulty in obtaining atomic resolution structures using an electron microscope with a high experimental B-factor. If, instead, a microscope with a mean B-factor of $\sim$50 $Å^2$ were used, a 5 Å structure would require a minimum of 50 000 particles. In this case, a 2-fold improvement in B-factor produces a 24-fold reduction in image collection and data processing requirements. This demonstrates the advantages of using a new generation of field emission gun microscopes with the smallest possible experimental B-factor. As these microscopes become more widely available and easy to use, the experimental limitations to achieving higher resolution can be minimized. However, the potential improvement in data collection will not be sufficient by itself and computational inaccuracies will also have to be reduced before reconstruction to near atomic resolution will become possible for single particles.

We thank Joyce Mitchell and David McNab for their technical assistance in preparing the virus samples. This research has been supported by NIH grants (RO1AI38469, P41RR02250) and the Robert Welch Foundation. The SSRL is funded by DOE BES and the SSRL Structural Biology Resource is funded by NIH (P41RR01209) and DOE BER.

REFERENCES

Böttcher, B., Wynne, S. A., and Crowther, R. A. (1997) Determination of the fold of the core protein of hepatitis B virus by electron cryomicroscopy, *Nature* **386,** 88–91.

Brink, J., and Chiu, W. (1991) Contrast analysis of cryo-images of *n*-paraffin recorded at 400 kV out to 2.1 Å resolution, *J. Microsc.* **161,** 279–295.

Chiu, W. (1978) Factors in high resolution biological structure analysis by conventional transmission electron microscopy, *Scanning Electron Microsc.* **1,** 569–580.

Conway, J. F., Cheng, N., Zlotnick, A., Wingfield, P. T., Stahl, S. J., and Steven, A. C. (1997) Visualization of a 4-helix bundle in the hepatitis B virus capsid by cryo-electron microscopy, *Nature* **386,** 91–94.

Conway, J. F., and Steven, A. C. (1999) Methods for reconstructing density maps of "single" particles from cryoelectron micrographs to subnanometer resolution, *J. Struct. Biol.* **128,** 106–118.

Crowther, R. A., Amos, L. A., Finch, J. T., DeRosier, D. J., and Klug, A. (1970) Three dimensional reconstructions of spherical viruses by Fourier synthesis from electron micrographs, *Nature* **226,** 421–425.

Downing, K. H., and Chiu, W. (1982) Effect of stray magnetic field on image resolution in transmission electron microscopy, *Ultramicroscopy* **5,** 351–356.

Erickson, H. P., and Klug, A. (1970) The Fourier transform of an electron micrograph: Effects of defocussing and aberrations, and implications for the use of underfocus contrast enhancement, *Phil. Trans. R. Soc. Lond. B* **261,** 105–118.

Frank, J. (1969) Nachweis von objektbewegungen im lichtoptischen diffraktogramm von elektronmikroskopischen aufnahmen, *Optik* **30,** 171–180.

Frank, J. (1973) The envelope of electron microscopic transfer functions for partially coherent illumination, *Optik* **38,** 519–536.

Frank, J. (1976) Determination of source size and energy spread from electron micrographs using the method of Young's fringes, *Optik* **44,** 379–391.

Glaeser, R. M. (1999) Review: Electron crystallography: Present excitement, a nod to the past, anticipating the future, *J. Struct. Biol.* **128,** 3–14.

Glaeser, R. M., and Downing, K. H. (1992) Assessment of resolution in biological electron crystallography, *Ultramicroscopy* **47,** 256–265.

Hanszen, K. J. (1971) The optical transfer theory of the electron microscope: Fundamental principles and applications, *in* (R. Barer and V. E. Cosslett, Eds.), *Advances in optical and electron microscopy* Vol. 4, pp. 1–84, Academic Press, New York.

Hanszen, K. J., and Trepte, L. (1971) Die kontrastubertragung im Elecktonmikroskop bei partiell koharenter beleuchtung, *Optik* **33,** 166–182.

Henderson, R. (1995) The potential and limitations of neutrons, electrons and X-rays for atomic resolution microscopy of unstained biological molecules, *Q. Rev. Biophys.* **28,** 171–193.

Henderson, R., Baldwin, J. M., Ceska, T. A., Zemlin, F., Beckmann, E., and Downing, K. H. (1990) Model for the structure of bacteriorhodopsin based on high-resolution electron cryomicroscopy, *J. Mol. Biol.* **213,** 899–929.

Kühlbrandt, W., Wang, D. N., and Fujiyoshi, Y. (1994) Atomic model of plant light-harvesting complex by electron crystallography, *Nature* **367,** 614–621.

Ludtke, S. J., Baldwin, P. R., and Chiu, W. (1999) EMAN: Semiautomated software for high resolution single particle reconstructions, *J. Struct. Biol.* **128,** 82–97.

Mancini, E. J., Clarke, M., Gowen, B. E., Rutten, T., and Fuller, S. D. (2000) Cryo-electron microscopy reveals the functional organization of an enveloped virus, Semliki Forest virus, *Mol. Cell.* **5,** 255–266.

Matadeen, R., Patwardhan, A., Gowen, B., Orlova, E. V., Pape, T., Cuff, M., Mueller, F., Brimacombe, R., and van Heel, M. (1999) The *E. coli* large ribosomal subunit at 7.5 Å resolution, *Structure* **7,** 1575–1583.

Murata, K., Mitsuoka, K., Hirai, T., Walz, T., Agre, P., Heymann, J. B., Engel, A., and Fujiyoshi, Y. (2000) Structural determinants of water permeation through aquaporin-1, *Nature* **407,** 599–605.

Nogales, E., Wolf, S. G., and Downing, K. H. (1998) Structure of

the alpha beta tubulin dimer by electron crystallography, *Nature* **391,** 199–203.

Thon, F. (1971) Phase contrast electron microscopy, *in* (U. Valdre, Ed.) Electron Microscopy in Material Sciences, pp. 571–625, Academic Press, New York.

Thuman-Commike, P. A., Tsuruta, H., Greene, B., Prevelige, P. E., King, J., and Chiu, W. (1999) Solution X-ray scattering based estimation of electron cryomicroscopy imaging parameters for reconstruction of virus particles, *Biophys. J.* **76,** 2249–2261.

Trus, B. L., Roden, R. B., Greenstone, H. L., Vrhel, M., Schiller, J., and Booy, F. P. (1997) Novel structural features of bovine papillomavirus capsid revealed by a three dimensional reconstruction to 9 Å resolution, *Nat. Struct. Biol.* **4,** 411–418.

Tsuruta, H., Brennan, S., Rek, Z. U., Irving, T. C., Tompkins, W. H., and Hodgson, K. O. (1998) A wide bandpass multilayer monochromator for biological small angle scattering and diffraction, *J. Appl. Phys.* **31,** 672–682.

Wade, R. H. (1992) A brief look at imaging and contrast transfer, *Ultramicroscopy* **46,** 145–156.

Wade, R. H., and Frank, J. (1977) Electron microscope transfer functions for partially coherent axial illumination and chromatic defocus spread, *Optik* **49,** 81–92.

Williams, D. B., and Carter, C.B. (1996) Transmission Electron Microscopy, Plenum, New York.

Zhou, Z. H., and Chiu, W. (1993) Prospects for using an IVEM with a FEG for imaging macromolecules towards atomic resolution, *Ultramicroscopy* **49,** 407–416.

Zhou, Z. H., Dougherty, M., Jakana, J., He, J., Rixon, F. J., and Chiu, W. (2000) Seeing the herpesvirus capsid at 8.5 Å, *Science* **288,** 877–880.

Zhou, Z. H., Hardt, S., Wang, B., Sherman, M. B., Jakana, J., and Chiu, W. (1996) CTF determination of images of ice-embedded single particles using a graphics interface, *J. Struct. Biol.* **116,** 216–222.

Zhu, J., Penczek, P. A., Schroder, R., and Frank, J. (1997) Three-dimensional reconstruction with contrast transfer function correction from energy-filtered cryoelectron micrographs: Procedure and application to the 70S Escherichia coli ribosome, *J. Struct. Biol.* **118,** 197–219.